



Introduction of amorphous TiO₂ coating layer to improve the lithium storage of SiO₂ nanospheres anode

Mengzhao Ding¹ · Jianguang Zhai¹ · Panjing Zeng² · Chaomin Zhang² · Yunxia Ping²

Received: 9 September 2021 / Revised: 22 December 2021 / Accepted: 27 December 2021 / Published online: 3 January 2022
© The Author(s), under exclusive licence to Springer-Verlag GmbH Germany, part of Springer Nature 2022

Abstract

Silicon dioxide (SiO₂) is considered a promising candidate to replace commercial graphite anodes in lithium-ion batteries (LIBs). However, poor electrical conductivity and drastic volume swing hinder it from practical applications. Smart surface coatings have been shown to be good examples of dramatically improved SiO₂ cycling performance. Herein, a SiO₂@amorphous TiO₂ (SiO₂@a-TiO₂) composite with core–shell structure was synthesized via a facile sol–gel method. The amorphous TiO₂ shell shows elastic behavior during lithium discharging and charging processes, maintaining high structural integrity. The resulting materials serve as LIBs anodes with superior lithium storage properties in terms of high initial capacity (1125 m Ah g⁻¹ at 0.1 A g⁻¹), good rate capability (387 m Ah g⁻¹ at 2 A g⁻¹), and excellent cycling stability (582 m Ah g⁻¹ was retained over 300 cycles at 0.1 A g⁻¹).

Keywords SiO₂@a-TiO₂ composite · Surface coating · Anode materials · Lithium-ion batteries

Introduction

To address the growing energy problem, various energy storage devices have been developed such as supercapacitors, solar cells, and sodium-ion batteries [1–3]. Among them, lithium-ion batteries dominate the market due to their high energy density, long cycle life, and eco-friendliness [4, 5]. However, the available commercial graphite anode has an inferior theoretical capacity and may generate the lithium dendrites on the surface of electrodes [6, 7]. In this regard, SiO₂ has been considered as the promising anode candidate owing to the low operating voltage, abundant natural resources, and its fivefold increase of theoretical capacity (1965 m Ah g⁻¹) [8, 9]. Nevertheless, the practical application of SiO₂ in LIBs is severely hampered by poor electrical conductivity and drastic volume change during lithiation/delithiation processes [10].

Great efforts have been made to enhance the stability and electrical conductivity of SiO₂, and nanostructured SiO₂ materials have been shown to possess better lithium insertion/extraction kinetics compared to bulk SiO₂ [11–13]. Another promising approach to achieve remarkable improvement in cycling stability is to obtain a core–shell structure by surface coating with conductive materials, which not only improves the conductivity of the electrode but also avoids direct contact between electrodes and electrolyte, thus reducing the uncontrollable growth of the solid electrolyte interphase (SEI) film [14, 15]. For instance, Jiang et al. prepared a SiO₂@C composite by molecular self-assembly method, which showed good rate capability (316 m Ah g⁻¹ at 0.4 A g⁻¹) [16]. Moreover, Dong and co-workers have proposed three-dimensional SiO₂/nitrogen-doped graphene aerogels, which achieve high cycling performance (1000 m Ah g⁻¹ at 0.1 A g⁻¹ after 100 cycles) [17]. In the case of most carbonaceous coating layers, however, it is usually frustrating that the low initial coulombic efficiency (ICE) and safety issues [18, 19]. As we know that TiO₂ undergoes only slight volume expansion upon lithiation (< 4%), and the resultant lithiated TiO₂ during discharge process can promote the electrical conductivity of the electrode [20]. Recently, outer layers of a-TiO₂ with structure elasticity is believed to be capable of maintaining structural integrity of SiO₂ anodes, and its

✉ Jianguang Zhai
ws_zhang@sues.edu.cn

¹ School of Materials Engineering, Shanghai University of Engineering Science, Shanghai 201620, China

² School of Mathematics, Physics and Statistics, Shanghai University of Engineering Science, Shanghai 201620, China

intrinsically isotropic and open active diffusion channels promote the mobility of Li^+ and the diffusion of ions and e^- , leading to high ion accessibility and enhanced power and energy density of the electrode materials [21, 22].

Inspired by the above, in this work, we synthesized core-shell structured $\text{SiO}_2@a\text{-TiO}_2$ composite by a simple sol-gel method. This intriguing structure possesses some advantages as follows: (a) the core of SiO_2 nanosphere contributes to high capacity; (b) the $a\text{-TiO}_2$ shell shows elastic behavior with strain relaxation, thereby maintaining the integrity of the anode and alleviating the volume change during discharging/charging processes. In addition, it provides large number of Li^+ and e^- diffusion channels to improve Li^+ availability and electrochemical reactivity. As expected, the $\text{SiO}_2@a\text{-TiO}_2$ electrode delivers a high ICE of 53% and adorable discharge capacity of 582 m Ah g^{-1} over 300 cycles at 0.1 A g^{-1} .

Experimental

Materials synthesis

The schematic diagram of the preparation process of $\text{SiO}_2@a\text{-TiO}_2$ composite is shown in Fig. 1. Precisely, 5.8 ml of ammonia solution (28 wt%) and 2 ml of deionized water were added into 60 ml of ethanol under magnetic stirring, and then 4 ml of tetraethyl orthosilicate (TEOS) dispersed

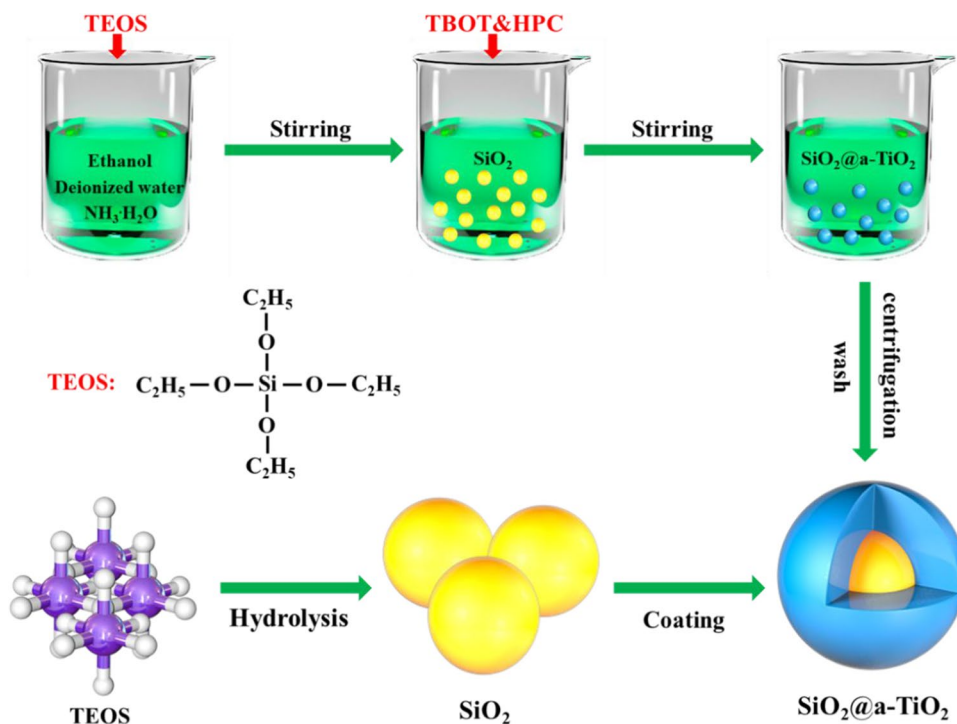
in 20 ml of ethanol was mixed into this solution. After stirring for 5 h, the white precipitate (SiO_2) was obtained by centrifugation and washed with deionized water and ethanol, respectively. Then, the collected SiO_2 precipitate was redispersed in 35 ml of ethanol, followed by the addition of 0.1 g hydroxypropyl cellulose (HPC) and 0.5 ml deionized water. Next, 1.2 ml of tetrabutyl titanate (TBOT) dissolved in 15 ml of ethanol was injected into the above solution and reacted at 80°C for 2 h. The resulting precipitate ($\text{SiO}_2@a\text{-TiO}_2$) was collected by centrifugation and washed with deionized water and ethanol, respectively. And in this composite, the weight percentage of $a\text{-TiO}_2$ can be calculated to be about 20.6%.

As a comparison, $\text{SiO}_2@\text{crystalline TiO}_2$ ($\text{SiO}_2@c\text{-TiO}_2$) composites were synthesized under a similar procedure with the additional process of calcination at 600°C for 3 h.

Materials characterization

The morphology and microstructure were analyzed with the scanning electron microscopy (SEM, Hitachi S4800) and transmission electron microscope (TEM, Tecnai-G2-F30 FEI with image corrector). The composition and crystal structure were characterized by X-ray diffraction measurement (XRD, Rigaku, D/max-Rbusing Cu K α radiation). The chemical state was investigated using an X-ray photoelectron spectroscope (XPS) (Thermo Scientific K-Alpha instrument with Al K α source).

Fig. 1 The schematic of preparing the core-shell $\text{SiO}_2@a\text{-TiO}_2$ composite



Electrochemical measurements

Electrochemical tests were performed using CR2032-type coin cells. The working electrodes were prepared by mixing the active materials, acetylene black and poly vinylidene fluoride (PVDF) in Nmethyl-2-pyrrolidone (NMP) with a weight ratio of 7:2:1 to form a slurry. The slurry was uniformly spread on a copper foil. Pure lithium foil was used as the counter electrode. Celgard2400 was used as separator. A 1 M solution of LiPF_6 dissolved in ethylene carbonate and dimethyl carbonate (1:1 in volume ratio) was used as the electrolyte. The lithium half-cells were assembled in an argon-filled glovebox with both water and oxygen levels below 0.1 ppm. Cyclic voltammetry (CV) data were recorded using an CHI760E electrochemical workstation. Electrochemical performance was collected on a Neware battery test system. Electrochemical impedance spectra (EIS) were also carried out on an CHI760E electrochemical workstation.

Results and discussion

The morphology and microstructure of the prepared samples were characterized by scanning electron microscopy (SEM) and transmission electron microscopy (TEM). As shown in Fig. 2a–c, these samples all exhibit a spherical structure with a uniform diameter of about 200 nm. Note that the surface of SiO_2 is relatively smooth compared to $\text{SiO}_2@a\text{-TiO}_2$, which indicates that a- TiO_2 is coated on the surface of the SiO_2 nanospheres. TEM image (Fig. 2d) also shows that the SiO_2 nanospheres display a size of about 200 nm, which is in good agreement with SEM image (Fig. 2a). Compared with the SiO_2 nanospheres, a uniform coating layer was observed on the surface of $\text{SiO}_2@a\text{-TiO}_2$ (Fig. 2e), and the thickness of a- TiO_2 is about 15 nm, which could be observed from Fig. S1 [23]. Figure 1f further shows the HRTEM image of $\text{SiO}_2@a\text{-TiO}_2$; there is no obvious lattice spacing corresponding to crystalline TiO_2 , indicating that the TiO_2 coating layer is amorphous. Elemental mapping results are

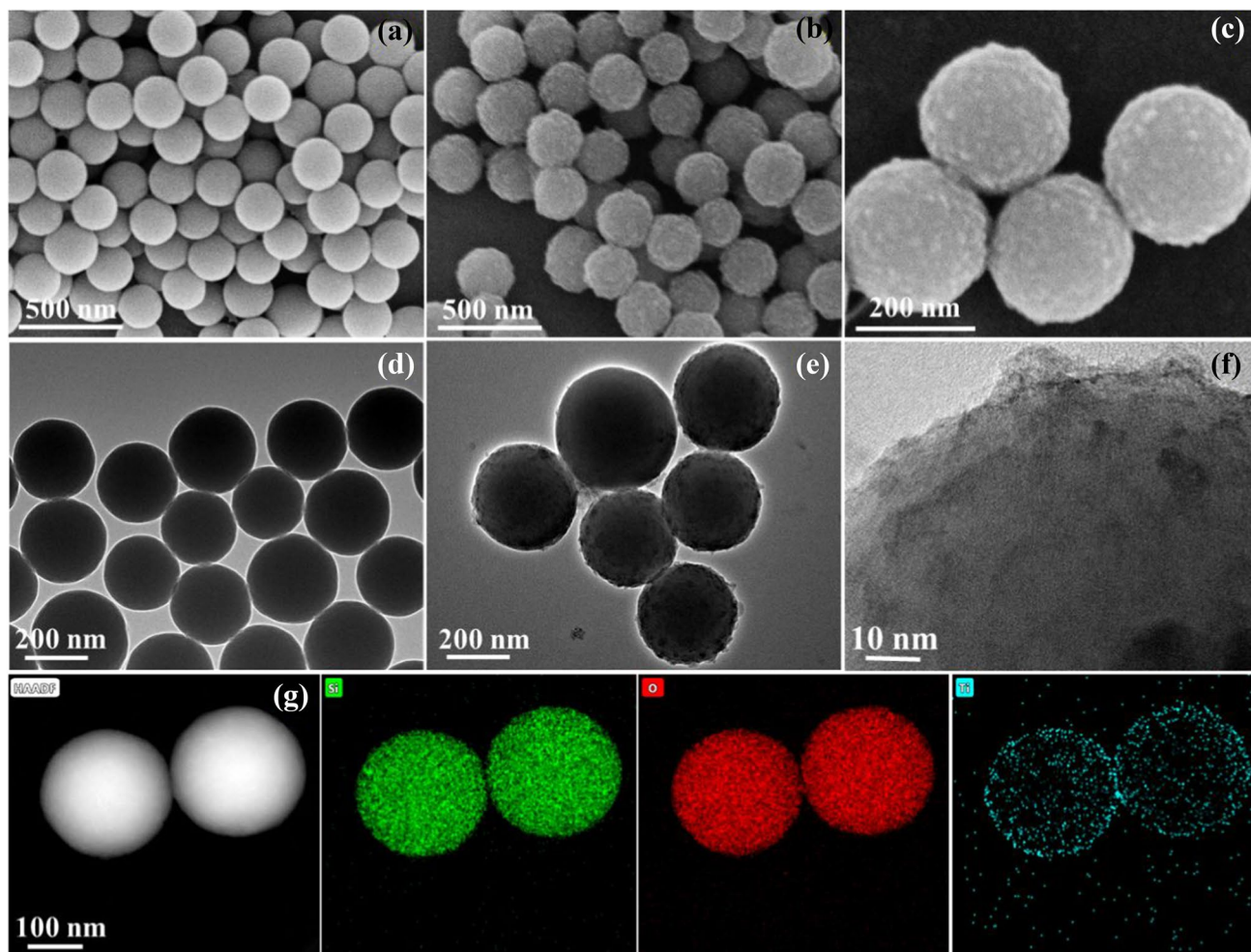


Fig. 2 SEM images of **a** SiO_2 and **b–c** $\text{SiO}_2@a\text{-TiO}_2$; TEM images of **d** SiO_2 and **e** $\text{SiO}_2@a\text{-TiO}_2$. **f** HRTEM image of $\text{SiO}_2@a\text{-TiO}_2$. **g** TEM image and corresponding elemental mappings (Si, O, and Ti elements) of $\text{SiO}_2@a\text{-TiO}_2$

displayed in Fig. 2g and reveal the uniform distribution of Si, O, and Ti in the SiO_2 @a- TiO_2 composite.

The XRD patterns are shown in Fig. 2c. Note that only a broad peak at 22.3° can be observed in the XRD pattern of SiO_2 , indicating its amorphous nature [24, 25]. In addition, no obvious diffraction peak can be detected from the pattern of SiO_2 @a- TiO_2 , demonstrating that the surface-coated TiO_2 shell is also amorphous. Moreover, several new diffraction peaks can be observed in the SiO_2 @c- TiO_2 composite pattern at 24.3° , 37.8° , 47.6° , 54.5° , and 55.3° , corresponding to the (101), (004), (200), (105), and (211) lattice planes of anatase TiO_2 (JCPDS no.21–1272), respectively, which proves that the a- TiO_2 is successfully converted into crystalline TiO_2 after the calcination process [26, 27]. XPS measurements were used to evaluate the chemical states of the elements in the SiO_2 and SiO_2 @a- TiO_2 composite. In the XPS survey spectra, several distinct peaks at ~ 103 , 154, 284, and 534 eV can be found, corresponding to Si 2p, Si 2s, C 1s, and O 1s of SiO_2 (Fig. 3b) [28, 29]. The C 1s peak may be assigned to tape substrate [30]. In contrast to the survey spectrum of SiO_2 , a unique peak of Ti 2p can be clearly noticed in the XPS survey spectrum of SiO_2 @a- TiO_2 composite, indicating that the SiO_2 cores are well encapsulated by the a- TiO_2 shells. The Si $2p_{3/2}$ peak is evidently prominent at 103.6 eV (Fig. 3c), corresponding to Si^{4+} . In addition, the high-resolution XPS spectrum shows Ti $2p_{3/2}$ and Ti $2p_{1/2}$ peaks of TiO_2 located at 458.2 and 464.6 eV (Fig. 3d) [31, 32].

The SiO_2 @a- TiO_2 composite was evaluated as anode materials for lithium storage properties in LIBs. The electrochemical redox reactions of this composite were studied by cyclic voltammetry from 0.01 and 3 V at a scan rate of 0.1 mV s^{-1} . Figure 4a shows the CV curves for the first three cycles, and it is obvious that a wide and weak cathodic peak appears about 1.46 V during the initial cycle, which could be caused by the irreversible reaction between Li^+ and SiO_2 as in Eqs. (1) and (2) [33]. In the subsequent lithiation process, broad cathodic peak at about 0.85 V and 0.56 V can be observed, which could be related to the side reaction of irreversible Li^+ insertion together with the formation of SEI film [34]. Another cathodic peak around 0 V corresponds to the alloy reaction between Li^+ and Si as in Eq. (3). In addition, two anodic peaks at about 0.25 and 1.05 V corresponding to de-alloy reaction can be observed in the subsequent delithiation process, as in Eq. (4) [35, 36].

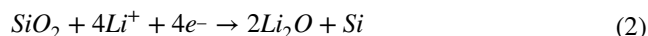
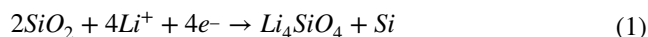


Fig. 3 **a** XRD patterns of SiO_2 , SiO_2 @c- TiO_2 , and SiO_2 @a- TiO_2 ; **b** full XPS spectrum of the SiO_2 and SiO_2 @a- TiO_2 ; **c** Ti 2p **e** and O1s **d** XPS high-resolution spectra of the SiO_2 @a- TiO_2

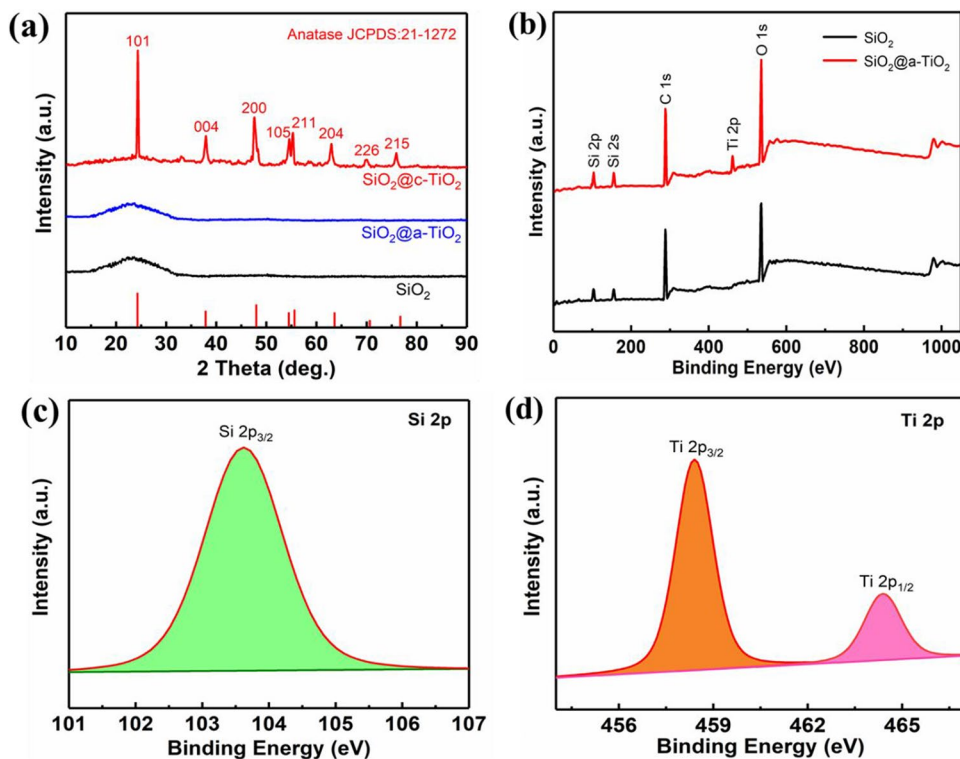


Fig. 4 **a** CV curves for the first three cycles of SiO₂@a-TiO₂ at 0.1 mV s⁻¹; **b** discharge and charge profiles for the 1st, 2nd, and 300th of SiO₂@a-TiO₂ at 0.1 A g⁻¹; **c** rate capability at different current rates, and **d** cycling performances and CE of SiO₂, SiO₂@c-TiO₂, and SiO₂@a-TiO₂ at 0.1 A g⁻¹

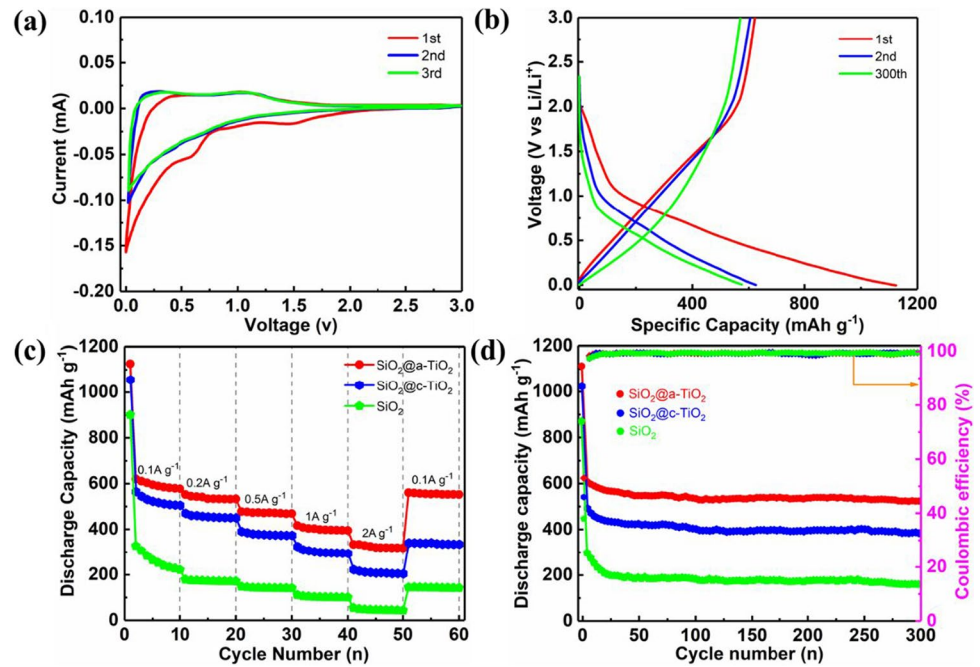


Figure 4b shows the 1st, 2nd, and 300th galvanostatic discharge/charge profiles of the SiO₂@a-TiO₂ composite. As can be observed, the composite delivers an initial discharge and charge capacity of 1125 m Ah g⁻¹ and 597 m Ah g⁻¹, respectively. Meanwhile, the initial discharge/charge capacity of SiO₂ and SiO₂@c-TiO₂ were 1046/481 m Ah g⁻¹ (Fig. S2a) and 891/338 m Ah g⁻¹ (Fig. S2b), respectively. These samples all suffered serious capacity loss, which could be caused by the irreversible reaction and the formation of SEI film. However, what is gratifying is that the SiO₂@a-TiO₂ composite also exhibits intriguing stability, with capacity retention of 92% from the 2nd to 300th cycle, which is superior to that 77.6% of SiO₂ and 63.8% of SiO₂@c-TiO₂. Figure 4c shows the rate curves of the three electrodes; it can be observed that the SiO₂@a-TiO₂ composite delivers discharge capacities of 581, 548, 472, and 395 m Ah g⁻¹ at current density of 0.1, 0.2, 0.5, and 1 A g⁻¹. Even at an ultrahigh current density of 2 A g⁻¹, it can still achieve a capacity of 387 m Ah g⁻¹, with a retention of 56% relative to the value at 0.1 A g⁻¹. Moreover, a discharge capacity of 578 m Ah g⁻¹ can be recovered when the current density goes back to 0.1 A g⁻¹, indicating the superior rate performance of the SiO₂@a-TiO₂ composite. The composite also exhibits excellent cycling performance as shown in Fig. 4d. It delivers an initial discharge capacity of 1125 m Ah g⁻¹, then decays to 580 m Ah g⁻¹ in the first 50 cycles, and remains very stable value of 572 m Ah g⁻¹ up to 300 cycles. In addition, SiO₂@a-TiO₂ composites

not only provide a high ICE of 53%, higher than that 37% of SiO₂ and 46% of SiO₂@c-TiO₂, but also maintain a stable CE value of nearly 100% over 2 to 300 cycles. The SiO₂@a-TiO₂ shows superior cycling performance than SiO₂ and SiO₂@c-TiO₂, resulting from the improvement of electrical conductivity and slighter volume variation of the electrode.

Electrochemical impedance spectroscopy measurements were also carried out on three samples to study the resistance property. Figure 5a shows the Nyquist plots and equivalent circuit; it is obvious that all the plots contain a semicircle in high- to middle-frequency region and an inclined line in low-frequency region, of which the diameter correlates with the charge transfer resistance at the electrodes and electrolyte interface (R_{ct}), and a low-frequency sloping line, which can associate with Warburg impedance (Z_w), is corresponding to the spread of Li⁺ in a large proportion of the electrode materials [37]. The simplified equivalent circuit for the simulation of EIS, in which R_s, R_{ct}, CPE, and W_o accordingly represent the solution resistance, charge transfer resistance, constant phase element, and Warburg resistance [38]. The fitting values of various electrodes are exhibited in Table 1. The value of R_s for each electrode is about 3 Ω. It is distinct that the SiO₂@a-TiO₂ has lower R_{ct} (80.5 Ω) comparing with SiO₂@c-TiO₂ (115.2 Ω) and SiO₂ nanospheres (132.6 Ω). In addition, as shown in Fig. 5b, the R_{ct} value of SiO₂@a-TiO₂ electrode slightly increased after cycling, indicating that a-TiO₂ could not only maintain the stable

Fig. 5 Nyquist plots of **a** SiO_2 , $\text{SiO}_2@c\text{-TiO}_2$, and $\text{SiO}_2@a\text{-TiO}_2$ before cycling, and **b** $\text{SiO}_2@a\text{-TiO}_2$ after cycling 1st, 50th, and 300th; **c** the line relationship of $Z' \sim \omega^{-1/2}$; **d** the diagram of battery

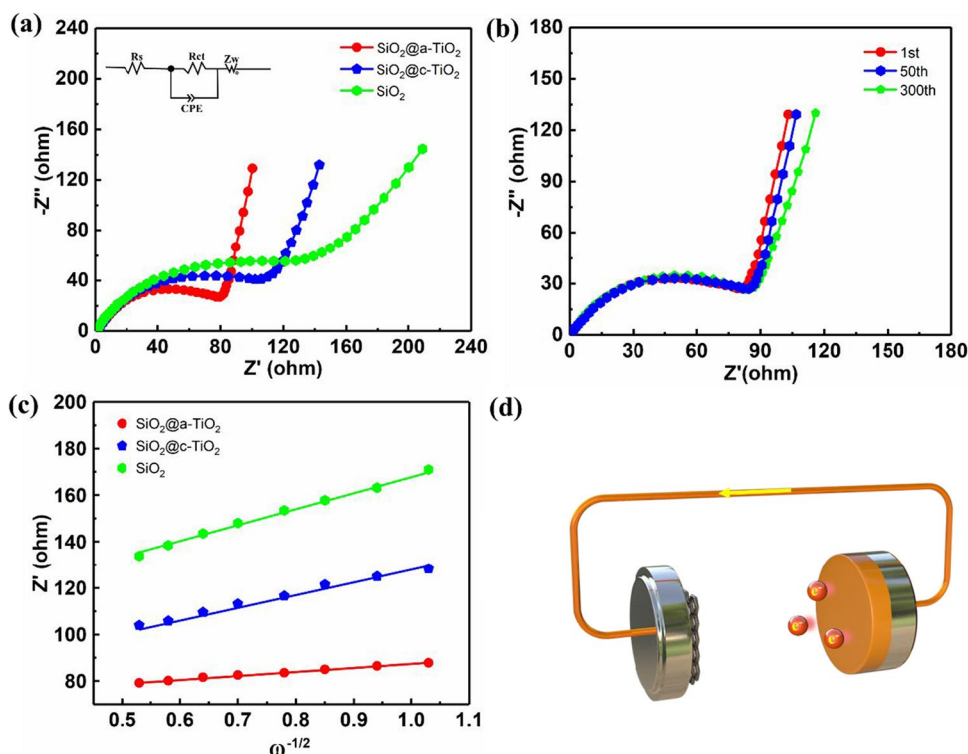


Table 1 Impedance parameters and lithium-ion diffusion coefficient of various electrode

Electrodes	R_s (Ω)	R_{ct} (Ω)	Slope	D_{Li^+} (cm^2s^{-1})
SiO_2	3.26	132.64	73.27	2.85×10^{-14}
$\text{SiO}_2@c\text{-TiO}_2$	3.15	115.28	45.54	7.38×10^{-14}
$\text{SiO}_2@a\text{-TiO}_2$	3.02	80.55	31.85	1.51×10^{-13}

structure of the electrode during cycling, but also ensure the rapid transport of Li^+ and e^- in the electrode.

The slope of the line located at the lower frequency corresponds to the diffusion process of Li^+ within the electrode [20]. And the D_{Li^+} of the corresponding sample can be calculated by Eqs. (5) and (6) [39].

$$D_{(\text{Li}^+)} = \frac{R^2 T^2}{2A^2 n^4 F^4 C^2 \sigma^2} \quad (5)$$

$$Z_{re} = R_{ct} + R_s + \sigma \omega^{-1/2} \quad (6)$$

where the R , T , A , and F stood for the gas constant, absolute temperature, surface area of the pole piece, and Faraday constant, respectively. C denoted the volume concentration of Li^+ . n represented the number of transferred electrons. For Eq. (4), σ donated the slope of Z_{re} and $\omega^{-1/2}$. The ω represents the angular frequency. As shown in Table 1, the

$\text{SiO}_2@a\text{-TiO}_2$ electrode possesses the highest D_{Li^+} value of 1.51×10^{-13} , which is superior to the value of the pure SiO_2 electrode (2.85×10^{-14}) and $\text{SiO}_2@c\text{-TiO}_2$ electrode (7.38×10^{-14}). The results may be attributed to the surface coating of $a\text{-TiO}_2$ with more diffusion channels, which is beneficial for improving the electrical conductivity of electrode by providing faster lithium ions transfer.

To further observe the structural changes of the electrodes during long-term cycling, the morphologies of the electrode surfaces of SiO_2 , $\text{SiO}_2@c\text{-TiO}_2$, and $\text{SiO}_2@a\text{-TiO}_2$ were investigated after 300 cycles, as shown in Fig. 6a–c. It can be clearly seen that more obvious and wider cracks appear on the electrode surfaces of SiO_2 and $\text{SiO}_2@c\text{-TiO}_2$ after long-term cycling. In contrast, the cracks of the $\text{SiO}_2@a\text{-TiO}_2$ electrode are much less and smaller than those of the other two electrodes. In addition, Figs. 6d–f show the microstructure of the high magnification images of the various electrodes, and it is obvious that there are distinct granules on the SiO_2 and $\text{SiO}_2@c\text{-TiO}_2$ electrodes, which may represent aggregates of electrode materials and conductive agents. The aggregation of powders leads to a non-uniform distribution on the electrode, which in turn loses contact with the conducting agent and leads to a decrease in electronic conductivity. Therefore, $a\text{-TiO}_2$ coating layer can effectively mitigate the volume expansion of SiO_2 and form a stable SEI film on the surface of SiO_2 . And a mechanism diagram of

Fig. 6 SEM images of **a** and **d** SiO₂, **b** and **e** SiO₂@c-TiO₂, and **c** and **f** SiO₂@a-TiO₂ after 300 cycles

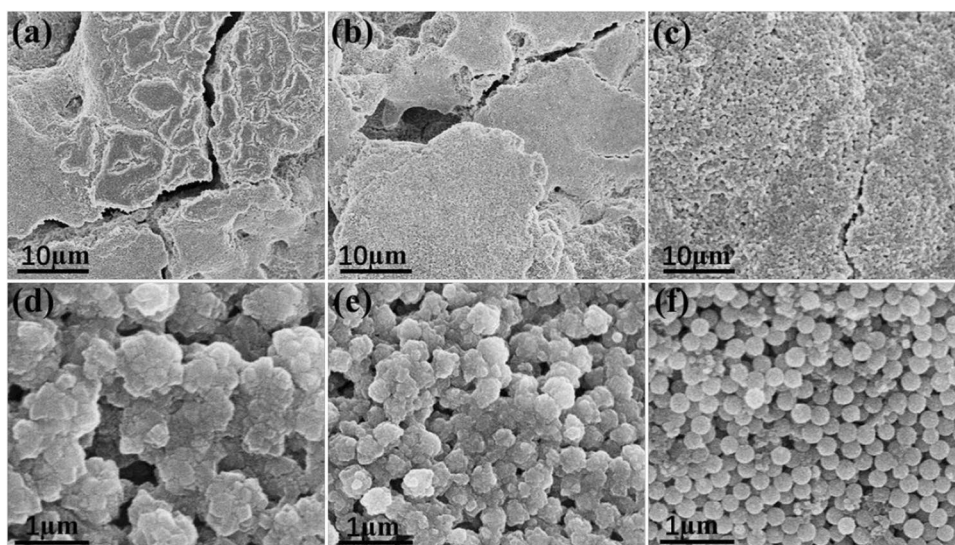
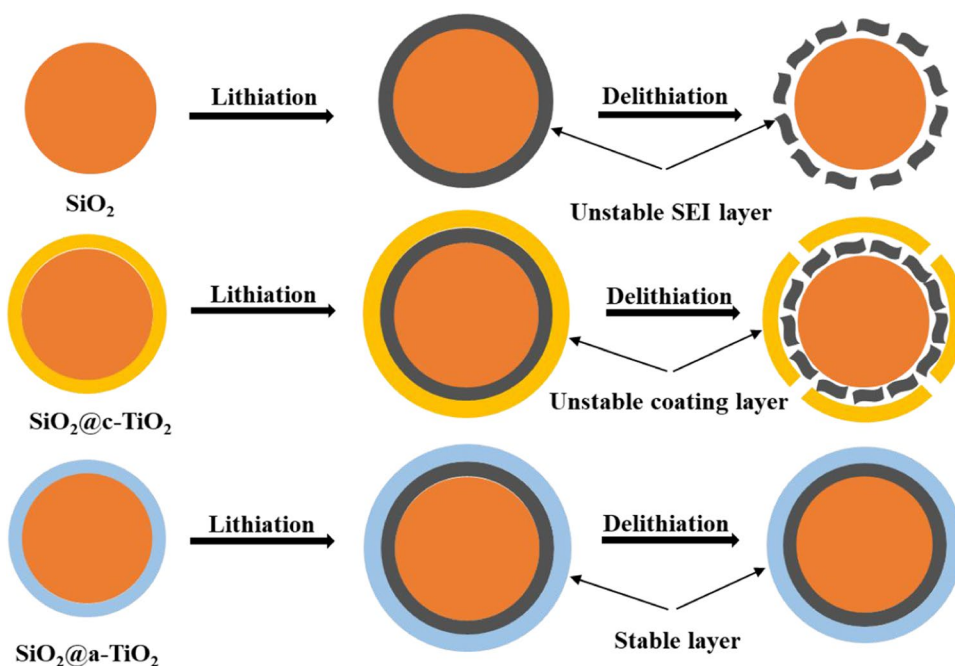


Fig. 7 Mechanism diagram of material surface of **a** SiO₂, **b** SiO₂@c-TiO₂, and **c** SiO₂@a-TiO₂



material surface on the performance of these electrodes is also demonstrated in Fig. 7.

Conclusion

In summary, the core–shell nano-structured SiO₂@a-TiO₂ composite was successfully obtained by sol–gel method. The composite, coated by a-TiO₂, which is beneficial for alleviating the volume expansion of SiO₂ and providing more diffusion channels for the transfer of Li⁺ and e⁻,

delivered excellent discharge capacity of 582 m Ah g⁻¹ at 0.1 A g⁻¹ after 300 cycles, and superior rate performance with a discharge capacity of 387 m Ah g⁻¹ at 2 A g⁻¹. These results demonstrated that nano SiO₂ coated with a-TiO₂ is promising anode materials for LIBs. In addition, this facial sol–gel synthetic route could inspire further capability on constructing core–shell structured materials for energy storage.

Supplementary Information The online version contains supplementary material available at <https://doi.org/10.1007/s11581-021-04435-w>.

Acknowledgements This work is supported by the National Natural Science Foundation of China (61604094).

References

- Feng HG, Xie P, Xue SL, Li LW, Hou X, Liu ZY, Wu DJ, Wang LW, Chu PK (2018) Synthesis of three-dimensional porous reduced graphene oxide hydrogel/carbon dots for high-performance supercapacitor. *J Electroanal Chem* 808:321–328
- Zhao WC, Li SS, Yao HF, Zhang SQ, Zhang Y, Yang B, Hou JH (2017) Molecular optimization enables over 13% efficiency in organic solar cells. *J Am Chem Soc* 139:7148–7151
- Hwang JY, Myung ST, Sun YK (2017) Sodium-ion batteries: present and future. *Chem Soc Rev* 46:3529–3614
- Zheng C, He C, Zhang H, Wang W, Lei X (2014) TiO₂ reduced graphene oxide nanocomposite for high-rate application of lithium ion batteries. *Ionics* 21:51–583
- Yang ZY, Yuan YF, Zhu M, Yin SM, Cheng JP, Guo SY (2021) Superior rate-capability and long-lifespan carbon nanotube-in-nanotube@Sb₂S₃ anode for lithium-ion storage. *J Mater Chem A* 9:22334–22346
- Kim YM, Ahn J, Yu SH, Chung DY, Lee KJ, Lee JL, Sung YE (2015) Titanium silicide coated porous silicon nanospheres as anode materials for lithium ion batteries. *Electrochim Acta* 151:256–262
- Sohn H, Kim DH, Yi R, Tang D, Lee SE, Jung YS, Wang D (2016) Semimicro-size agglomerate structured silicon-carbon composite as an anode material for high performance lithium-ion batteries. *J Power Sources* 334:128–136
- Yu Y, Zhan ZH, Xu QY, Shen K (2020) Dual stabilized architecture of Si@SiO₂/N-doped carbon composite synthesized via oxygen plasma method as anode for high-performance LIBs. *Chem Lett* 49:423–427
- Wu W, Wang M, Wang J, Wang CY, Deng YH (2020) Green design of Si/SiO₂/C composites as high-performance anodes for lithium-ion batteries. *ACS Appl Energy Mater* 3:3884–3892
- Nan D, Wang JG, Huang ZH, Wang L, Shen WC, Kang FY (2013) Highly porous carbon nanofibers from electrospun polyimide/SiO₂ hybrids as an improved anode for lithium-ion batteries. *Electrochem Commun* 34:52–55
- Zheng H, Wang ZY, Shi LY, Zhao Y, Yuan S (2019) Enhanced thermal stability and lithium ion conductivity of polyethylene separator by coating colloidal SiO₂ nanoparticles with porous shell. *J Colloid Interface Sci* 554:29–38
- Wu JH, Zuo XX, Chen QY, Deng X, Liang HY, Zhu TM, Liu JS, Li WJ, Nan JM (2019) *Electrochim Acta* 320:134567
- Ensafi AA, Abarghoui MM, Rezaei B (2017) Metal (Ni and Bi) coated porous silicon nanostructure, high-performance anode materials for lithium ion batteries with high capacity and stability. *J Alloys Compd* 712:233–240
- Xiang Z, Chen Y, Li J, Xia X, He Y, Liu H (2017) Submicro-sized porous SiO₂/C and SiO₂/C/graphene spheres for lithium ion batteries. *J Solid State Electrochem* 21:2425–2432
- Wang J, Hou X, Zhang M, Li Y, Wu Y, Liu X, Hu S (2016) 3-Aminopropyltriethoxysilane-assisted Si@SiO₂/CNTs hybrid microspheres as superior anode materials for Li-ion batteries. *SILICON* 9:97–104
- Jiang YH, Wen J, Ding ZW, Ren Y, Liu Z, Chen X, Zhou XW (2021) Li⁺ storage properties of SiO₂@C core-shell submicrosphere and its hollow counterpart synthesized by molecular self-assembly in wet chemistry condition as anodes for LIBs. *J Alloys Compd* 861:157932
- Dong XY, Zheng X, Deng YC, Wang LF, Hong HP, Ju ZC (2020) SiO₂/N-doped graphene aerogel composite anode for lithium-ion batteries. *J Mater Sci* 55:13023–13035
- Chen H, Hou X, Chen F, Wang S, Bo W, Qiang R (2018) Milled flake graphite/plasma nano-silicon@carbon composite with void sandwich structure for high performance as lithium ion battery anode at high temperature. *Carbon* 130:433–440
- Shen X, Tian Z, Fan R, Shao L, Zhang D, Cao G, Kou L, Bai Y (2018) Research progress on silicon/carbon composite anode materials for lithium-ion battery. *J Energy Chem* 27:1067–1090
- Fang R, Xiao W, Miao C, Mei P, Zhang Y, Yan XM, Jiang Y (2019) Enhanced lithium storage performance of core-shell structural Si@TiO₂/NC composite anode via facile sol-gel and in situ N-doped carbon coating processes. *Electrochim Acta* 317:575–582
- Majeed MK, Saleem A, Ma XJ, Ma WZ (2020) Clay-derived mesoporous Si/rGO for anode material of lithium-ion batteries. *J Alloys Compd* 848:156590
- Xiao ZX, Yu CH, Lin XQ, Chen X, Zhang CX, Jiang HR, Zhang RF, Wei F (2020) TiO₂ as a multifunction coating layer to enhance the electrochemical performance of SiO_x@TiO₂@C composite as anode material. *Nano Energy* 77:105082
- Feng K, Li M, Liu W, Kashkooli AG, Xiao X, Cai M, Chen Z (2018) Silicon-based anodes for lithium-ion batteries: from fundamentals to practical applications. *Small* 14:1702737
- Zhu Y, Hu W, Zhou J, Cai W, Lu Y, Liang J, Li X, Zhu S, Fu Q, Qian Y (2019) Pre-lithiated surface oxide layer enabled high-performance Si anode for lithium storage. *ACS Appl Mater Inter* 11:18305–18312
- Su J, Zhao J, Li L, Zhang C, Chen C, Huang T, Yu A (2017) Three-dimensional porous Si and SiO₂ with in situ decorated carbon nanotubes as anode materials for Li-ion batteries. *ACS Appl Mater Inter* 9:17807–17813
- Liang J, Han X, Li Y, Ye K, Hou C, Yu K (2015) Fabrication of TiO₂ hollow nanocrystals through the nanoscale Kirkendall effect for lithium-ion batteries and photocatalysis. *New J Chem* 39:3145–3149
- Yuan YF, Zhao WC, Chen L, Cai GS, Guo SY (2021) CoO hierarchical mesoporous nanospheres@TiO₂@C for high-performance lithium-ion storage. *Appl Surf Sci* 556:149810
- Majeed MK, Ma G, Cao Y, Mao H, Ma X, Ma W (2019) Metal-organic frameworks derived mesoporous Si/SiO_x@NC nanospheres as a long-lifespan anode material for lithium-ion batteries. *Chem Eur J* 25:11991–11997
- Lee G, Kim S, Kim S, Choi J (2017) SiO₂/TiO₂ composite film for high capacity and excellent cycling stability in lithium-ion battery anodes. *Adv Funct Mater* 27:1703538
- Lv P, Zhao H, Wang J, Liu X, Zhang T, Xia Q (2013) Facile preparation and electrochemical properties of amorphous SiO₂/C composite as anode material for lithium ion batteries. *J Power Sources* 237:291–294
- Smith KA, Savva AI, Mao KYS, Wang YQ, Tenne DA, Chen D, Liu YZ, Barnes P, Deng CJ, Butt DP, Wharry JP, Xiong H (2019) Effect of proton irradiation on anatase TiO₂ nanotube anodes for lithium-ion batteries. *J Mater Sci* 54:13221–13235
- Subasi Y, Somer M, Yagci MB, Slabon A, Afyon S (2020) Surface modified TiO₂/reduced graphene oxide nanocomposite anodes for lithium ion batteries. *J Solid State Electrochem* 24:1085–1093
- Shen Y, Cao Z, Wu Y, Cheng Y, Xue H, Zou Y, Liu G, Yin D, Cavallo L, Wang L, Ming J (2020) Catalysis of silica-based anode (de-)lithiation: compositional design within a hollow structure for accelerated conversion reaction kinetics. *J Mater Chem* 8:12306–12313
- Wang H, Cai W, Wang S, Li B, Yang Y, Li Y, Wu QH (2020) Fabrication of helical SiO₂@Fe-N doped C nanofibers and their

- applications as stable lithium ion battery anodes and superior oxygen reduction reaction catalysts. *Electrochim Acta* 342:136107
35. Ali S, Jaffer S, Maitlo I, Shehzad FK, Wang Q, Ali S, Akram MY, He Y, Nie J (2020) Photo cured 3D porous silica-carbon (SiO₂-C) membrane as anode material for high performance rechargeable Li-ion batteries. *J Alloys Compd* 812:152127
 36. Yang JP, Wang YX, Li W, Wang LJ, Fan YC, Jiang W, Luo W, Wang Y, Kong B, Selomulya C, Liu HK, Dou SX, Zhao DY (2017) Amorphous TiO₂ shells: a vital elastic buffering layer on silicon nanoparticles for high performance and safe lithium storage. *Adv Mater* 29:1700523
 37. Zhang J, Liang Y, Zhou Q, Peng Y, Yang H (2015) Enhancing electrochemical properties of silicon-graphite anodes by the introduction of cobalt for lithium ion batteries. *J Power Sources* 290:71–79
 38. Yuan YF, Chen Q, Zhu M, Cai GS, Guo SY (2021) Nano tube-in-tube CNT@void@TiO₂@C with excellent ultrahigh rate capability and long cycling stability for lithium ion storage. *J Alloys Compd* 851:156795
 39. Zhou N, Wu YF, Li YR, Yang JK, Zhou Q, Guo YW, Xia M, Zhou Z (2020) Interconnected structure Si@TiO₂-B/CNTs composite anode applied for high-energy lithium-ion batteries. *Appl Surf Sci* 500:144026

Publisher's note Springer Nature remains neutral with regard to jurisdictional claims in published maps and institutional affiliations.